

Sunyaev Zel’dovich observations of a statistically complete sample of galaxy clusters with OCRA-p

Katy Lancaster¹, Mark Birkinshaw¹, Marcin P. Gawroński²,
Richard Battye³, Ian Browne³, Richard Davis³, Paul Giles¹, Roman Feiler²,
Andrzej Kus², Bartosz Lew², Stuart Lowe³, Ben Maughan¹, Abdulaziz Mohammad¹,
Bogna Pazderska², Eugeniusz Pazderski², Mike Peel³, Boud Roukema²
and Peter Wilkinson³

¹ *H. H. Wills Physics Laboratory, University of Bristol, Tyndall Avenue, Bristol BS8 1TL*

² *Toruń Centre for Astronomy, Nicolaus Copernicus University, ul. Gagarina 11, 87-100 Toruń, Poland*

³ *Jodrell Bank Centre for Astrophysics, The University of Manchester, Alan Turing Building, Manchester M13 9PL*

Received **insert**, Accepted **insert**

ABSTRACT

We present 30 GHz Sunyaev Zel’dovich observations of a statistically complete sample of galaxy clusters with OCRA-p. The clusters are the 18 most X-ray luminous clusters at $z > 0.2$ in the ROSAT Brightest Cluster Sample. We correct for contaminant radio sources via supplementary observations with the Green Bank Telescope, also at 30 GHz, and remove a cluster that is contaminated by an unresolved X-ray source. All 17 remaining clusters have central SZ effects with Comptonisation parameter y_0 exceeding 1.9×10^{-4} , and 13 are detected at significance $\geq 3\sigma$. We use our data to examine scalings between y_0 and X-ray temperature, X-ray luminosity, and the X-ray mass proxy Y_X , and find good agreement with predictions from self-similar models of cluster formation, with an intrinsic scatter in y_0 of about 25%. We also comment on the success of the observations in the face of the contaminant source population, and the implications for upcoming cm-wave surveys.

Key words: cosmology: observations – cosmic microwave background – galaxies: clusters: individual (A1835, ZWCL1953, A689, ZWCL3146, RXJ1532.9+3021, A2390, A2219, RXJ2129.6+0005, A2261, A781, A697, A1763, A68, A520, A267, RXJ0439.0+0715, ZWCL7160, A773) – methods: observational

1 INTRODUCTION

The thermal Sunyaev Zel’dovich (SZ) effect (Sunyaev & Zel’dovich 1972) is a spectral distortion of the Cosmic Microwave Background (CMB) radiation due to inverse Compton scattering by the hot gas in galaxy clusters. It has long been exploited in cosmological and cluster studies in order to derive, for example, the Hubble constant (e.g. Hughes & Birkinshaw 1998, Mason et al. 2001, Reese et al. 2002, Saunders et al. 2003, Bonamente et al. 2006) and the gas mass fraction (e.g. Grego et al. 2001, Lancaster et al. 2005, LaRoque et al. 2006). Thanks to well developed techniques, detections are becoming routine although signal-to-noise remains quite poor. However, we are entering an era of purpose-built instruments so this is set to improve dramatically, enabling SZ research to reach its evident potential.

The main focus of the SZ community at present is to utilise the redshift-independence of the SZ surface brightness in order to perform blind surveys for galaxy clusters. While other techniques suffer from large intrinsic biases and complex selection effects, SZ surveys will produce almost *mass-limited* catalogues and thus far superior datasets for constraining cosmological models. The dedicated SZ surveys, for example Planck (Ade et al. 2011), SPT (Staniszewski et al. 2009, Vanderlinde et al. 2010), ACT (Menanteau et al. 2010, Marriage et al. 2010) and the SZA (Muchovej et al. 2011) are now generating results. Many more are expected in the near future, e.g. from AMI (Zwart et al. 2008). In order to fully exploit the results of these surveys, it will be necessary to improve understanding of both the ‘selection effect’ due to the presence of unsubtracted radio sources, and also the scalings between cluster SZ observ-

ables and various physical quantities, especially the cluster mass. Various groups have undertaken similar studies (e.g. Benson et al. 2004, Morandi et al. 2007, Bonamente et al. 2008, Huang et al. 2010). To make further advances, reliable observations of large, well-selected samples are required.

The One Centimetre Receiver Array prototype, OCRA-p, is a two-element receiver mounted on the 32-m telescope at the Toruń Centre for Astronomy of the Nicolaus Copernicus University, Poland. OCRA-p proved its SZ capabilities by detecting four well known clusters at high significance (Lancaster et al. 2007). We present the first in a series of papers discussing an X-ray selected sample of 33 clusters with well understood selection effects. This paper contains details of our OCRA-p observations of a statistically complete subsample of 18 clusters. The structure of the paper is as follows. In Section 2 we give a brief description of the Toruń 32-m telescope and the OCRA-p receiver. Section 3 contains details of the cluster sample. The observations and data reduction are described in Section 4, and the problem of radio source contamination is detailed in Section 5. Section 6 gives a brief overview of our X-ray analysis, and Section 7 presents our results. We discuss these results and conclude in Section 8. Throughout the paper we adopt the following cosmological parameter values: $H_0 = 70 \text{ km s}^{-1} \text{ Mpc}^{-1}$, $\Omega_{m0} = 0.3$, $\Omega_{\Lambda 0} = 0.7$.

2 THE TORUN TELESCOPE AND OCRA-P

The Toruń observatory is located in Piwnice, 15 km outside Toruń in northern Poland. The telescope consists of a 32-m parabolic dish and 3.2-m sub-reflector, with a fully steerable classical Alt-Az mount. It has receivers operating at 1.4-1.7, 5, 6.8, 12 and 30 GHz. The telescope is used for a variety of studies including interstellar molecular spectroscopy (e.g. Błaszkiewicz & Kus 2004) and VLBI (e.g. Bartkiewicz et al. 2005).

OCRA is a planned 30 GHz 100-element continuum receiver (see Browne et al. 2000). A prototype receiver, OCRA-p, funded by a grant from the Royal Society Paul Instrument fund, has been on the telescope since 2004. The instrument is described in detail in Lowe (2005) and Lowe et al. (2007); here we present a short summary. The basic radiometer design is based on the prototype for the Planck Low Frequency Instrument (LFI, Mandolesi et al. 2000), and is similar to the WMAP K-band receivers (Jarosik et al. 2003). OCRA-p provides only two horn-feeds, the beams of which are separated by $3'.1$ and have FWHM $1'.2$. As the beam separation is small, it is possible to reduce the effects of atmospheric and gain fluctuations by switching between the beams and taking the difference. This can be improved upon by further levels of switching. The full switching strategy for SZ observations is described in Section 4.1. In addition to the SZ program, OCRA-p has been used to study planetary nebulae (Pazderska et al. 2009) and for various radio source studies including flux density measurements to support the Very Small Array CMB program (see Gawroński et al. 2010 for details of the OCRA measurements, and Genova-Santos et al. (in preparation) for the details of the CMB work). The next phase of the project is an 8-element array, OCRA-Faraday (Peel 2009), which was mounted on the telescope in late 2009. This is still in the commissioning phase but is

expected to be fully operational in autumn 2011, and can be upgraded to 16 elements in the future.

3 THE CLUSTER SAMPLE

In order to derive meaningful cosmological results, or indeed to comment on universal cluster properties, it is necessary to use a ‘fair’ sample, or at least one where the selection biases are clear and well understood. Large samples fulfilling these criteria are rare in SZ astronomy, largely due to the various practical challenges which observers must overcome. In this work, we attempt to select and observe such a sample, and turn to the ROSAT All-Sky Survey in the first instance.

The Brightest Cluster Sample (BCS, Ebeling et al. 1998) is derived from a careful analysis of the ROSAT All-Sky Survey (RASS, Voges et al. 1999) data at $\delta > 0^\circ$. The resulting catalogue is 90% flux complete to a limit of $f_X = 4.4 \times 10^{-12} \text{ erg cm}^{-2} \text{ s}^{-1}$ in the 0.1-2.4 keV energy band. Since the SZ surface brightness of a cluster is essentially unaffected by redshift, we select on luminosity, imposing a limit of $L_X \geq 13.08 \times 10^{44} \text{ erg s}^{-1}$ (the luminosity of A773 in the BCS catalogue). In addition, we impose the criterion $z > 0.2$ due to the $3'.1$ beam-throw of OCRA; observations at lower redshift are inefficient with this instrument. Our basic sample then consists of 18 clusters. We do not reject any clusters based on their radio-source environments at this stage, even though we appreciate the difficulties which this policy may introduce. This has the advantage of allowing us to investigate any correlation between gas properties and those of a central radio galaxy.

We reject one cluster from the basic 18-cluster sample, A689, as on further investigation we have found that the ROSAT data are contaminated by a bright central point source (Giles et al., in preparation). After removing this source from the *Chandra* data, the luminosity is just $(1.66 \pm 0.24) \times 10^{44} \text{ erg s}^{-1}$, more than a factor 8 below the limiting luminosity of the cluster sample. The sample is summarised in Table 1. These clusters appear not to be exceptional in their X-ray structures, and, indeed, follow the expected X-ray scaling relations (see Section 7.3).

4 OCRA DATA

4.1 Observing Strategy

The clusters were observed in good weather periods between September 2005 and January 2009. We aimed to achieve a uniform noise level $< 0.5 \text{ mJy}$, which required ~ 220 minutes of data at each pointing centre. Trail fields, blank patches of sky separated from the target fields by 15–20m in RA, were observed over the same range of hour angle after each cluster observation, using the same position switching routine (described below) as for the cluster fields. The integration times for the target and trail fields are identical.

For each observation, whether the cluster or its corresponding trail field, we employ a position switching strategy to remove atmospheric contamination from our data. The feeds are positioned such that one beam, beam *B*, is coincident with the cluster centre and the other, beam *A*, provides a measure of the blank sky signal. (For extended sources, beam *A* may measure a small signal itself. This

Table 1. Initial cluster parameters. Coordinates correspond to the OCRA pointing centres which in some cases were shifted slightly to avoid bright point sources. Δ RA and Δ Dec are the offsets from the maxima of the X-ray surface brightness in the *Chandra* data. L_X values refer to the 0.1–2.4 keV ROSAT energy band and are taken from Ebeling et al. (1998) along with the redshifts. A689 was originally in the sample, but on closer inspection it was found to have significant X-ray point source contamination. Once this was removed, the cluster luminosity fell to the bracketed value, well below our selection limit of $13.02 \times 10^{44} \text{ erg s}^{-1}$.

Cluster	RA (J2000)	Dec (J2000)	Δ RA (arcmin)	Δ Dec (arcmin)	z	L_X ($10^{44} \text{ erg s}^{-1}$)
A1835	14 01 01.99	02 53 12.8	0.02	0.53	0.25	38.53
ZWCL1953	08 50 03.00	36 04 16.0	-0.80	-0.04	0.32	34.12
A689	08 37 25.01	14 59 40.9	-	-	0.28	30.41 (1.66)
ZWCL3146	10 23 35.98	04 11 56.0	-0.90	0.75	0.29	26.47
RXJ1532.9+3021	15 32 58.99	30 21 11.2	1.13	0.20	0.35	24.40
A2390	21 53 34.61	17 40 10.9	-0.50	-1.56	0.23	21.44
A2219	16 40 21.80	46 42 47.8	0.24	0.30	0.23	20.40
RXJ2129.6+0005	21 29 40.50	00 05 49.9	0.11	0.51	0.24	18.59
A2261	17 22 27.00	32 07 04.1	-0.03	-0.88	0.22	18.18
A781	09 20 25.99	30 29 57.8	-0.04	-0.11	0.30	17.22
A697	08 42 58.01	36 21 45.0	0.03	-0.20	0.28	16.30
A1763	13 35 23.21	41 00 04.0	0.04	0.08	0.22	14.93
A68	00 37 05.30	09 09 10.8	-0.20	-0.38	0.26	14.89
A520	04 54 19.01	02 56 48.1	0.00	0.00	0.20	14.44
A267	01 52 42.00	01 00 25.9	-0.02	-0.24	0.23	13.71
RXJ0439.0+0715	04 39 01.01	07 16 54.8	0.08	0.85	0.23	13.25
ZWCL7160	14 57 19.99	22 20 35.9	1.13	0.03	0.26	13.19
A773	09 17 51.00	51 43 19.9	-0.32	-0.34	0.22	13.08

must be properly accounted for - see Section 6.2.) We switch between the *A* and *B* beams at a rate of 277 kHz, recording the *A* – *B* difference every second. We integrate in this position for 25 seconds. The telescope then slews to reposition the beams such that beam *A* measures the cluster and beam *B* measures the sky background, and the differencing is repeated, this time integrating for 50 seconds. We then return to the starting position and integrate for another 25 seconds. The differenced signals from the first and third positions, ($A_1 - B_1$) and ($A_3 - B_3$) are summed, and then subtracted from the differenced signal from the second position ($A_2 - B_2$). This recovers twice the cluster signal relative to the background regions. The symmetric nature of the switching pattern ensures proper subtraction of most atmospheric emission and other contaminants such as ground pick-up, provided that the target region is not rapidly changing in azimuth and elevation.

4.2 Calibration

The data are calibrated against an internal noise source, which is itself calibrated via observations of the well-known bright radio source NGC7027 of flux density 5.37 Jy. We observe significant changes in the level of the noise source in the form of: (a) sudden ‘jumps’, sometimes due to the telescope reconfiguration and (b) additional smaller amplitude fluctuations which appear random in nature. We note that other than the low-amplitude random fluctuations, the voltage level is generally stable on timescales of a few days. By performing regular calibration (\approx daily) we reduce the effects of the larger fluctuations. In addition, we adopt a conservative approach by comparing the total powers for the NGC7027 and cluster observations and rejecting any data for which they differ significantly, although a study suggests the calibration often stays virtually the same as the total

power drifts. Residual uncertainties in the calibration of the system at the level of 5% may be expected.

The telescope pointing is calibrated via azimuth and elevation scans across a bright source close to each cluster. Where an acceptable pointing calibration does not exist within 60 minutes of a cluster observation, the cluster data are rejected.

4.3 Statistical Data Analysis

After combination of the second-by-second average data into double-differenced measurements of the brightness of the sky, and calibration, the data are examined for periods of increased noise (which might arise from receiver instabilities or bad weather conditions) or individual anomalous points. The combination of the data into final averages was performed including statistical tests for outlier data. The fractions of the data points rejected by 3σ or 5σ cuts were small in all cases, and no cut-dependent changes larger than a small fraction of the error on the mean were seen. The distributions of data values in the double-difference data are close to Gaussian, with a slight tendency to show elevated wings in the distributions: the estimates of the error on the mean (Table 5) take account of the full distribution, and not the distribution after truncation of outliers.

5 RADIO SOURCE CONTAMINATION

Radio source contamination remains a significant problem for observations of the Sunyaev Zel’dovich effect. If we know the positions and 30 GHz flux densities of all sources near our observing locations, we can correct the data and establish the true magnitude of the SZ effect for each cluster. Ideally, we would consult a survey of the radio sky at a frequency close to 30 GHz in order to identify contaminant radio sources. The only such survey currently available is

the WMAP point source catalogue (Wright et al. 2009), but this is complete only to the 2 Jy level and so is three orders of magnitude too shallow for our purposes. We consult the all-sky NVSS (Condon et al. 1998, 1.4 GHz) and GB6 (Gregory et al. 1996, 4.85 GHz) catalogues and retain all sources within $5'$ of the pointing centre for each cluster. In addition, we include any sources found in similar projects and reported in the literature. The list of 58 contaminating sources is presented in Table 2.

5.1 GBT observations

We observed the 58 sources over the course of several sessions at the Green Bank Telescope (GBT) in January 2008 (observations limited due to poor weather conditions), then January and May 2009 (re-scheduled time, again compromised in part by non-ideal conditions). We used the GBT Ka-band receiver and the Caltech Continuum Backend (CCB). For a detailed description of this configuration of equipment and the observing methods used, see Mason et al. (2009); we will describe the salient points.

5.1.1 Calibration

Every observing session included at least one flux calibration observation, using the most accessible of the GBT standard calibrators 3C 147, 3C 48 or 3C 286. We observed sources cluster by cluster, and thus they tend to lie in small regions. The GBT pointing is stable for up to 40 minutes for night time observing, but we rarely required re-pointing near a field because slews tended to occur after only a few source integrations. We chose one pointing calibrator per cluster (and hence its associated sources). We took pointing calibrators from the GBT database, choosing the brightest available within 10 degrees of the cluster centre. We also performed at least one sky dip per observing session to establish the sky temperature and opacity.

5.1.2 Differencing

We employed the standard GBT nodding strategy, which is similar to the OCRA differencing scheme, in order to remove atmospheric contamination. A complete nod (ie the sequence of beam 1 on source, beam 2 on source, beam 2 on source, beam 1 on source) takes 1.5 minutes. Each source was observed for at least one complete nod. The number of nods was governed by telescope scheduling, though we tried to include extra nods for sources expected to have lower flux densities.

5.1.3 GBT flux density determinations

The CCB has a 14 GHz bandwidth, split into four frequency sub-bands centred at 27.75, 31.25, 34.75 and 38.25 GHz. We can thus measure simultaneously four separate flux densities for each source, from which we can derive a 30 GHz value by fitting a power law to the available data. We use a Monte-Carlo method to estimate the uncertainties on the interpolated flux densities. For poor-quality data, we were unable to derive accurate 30 GHz flux densities from the GBT data alone, as discussed in Section 5.2

5.2 Determining the 30 GHz flux densities

The quality of our GBT data is rather mixed due to the wide range of observing conditions experienced. As most sources were only observed once, we are also unable to constrain source variability with GBT data alone. In order to supplement our 30 GHz measurements, we make use of the flux densities reported in Coble et al. (2007) who observed all of our clusters except Abell 2390 at 28.5 GHz with the OVRO and BIMA interferometers. Such interferometric data not only measure the SZ effect but also enable identification of point sources via the longest baselines, where the SZ signal will be negligible. The uncertainties on the Coble et al. flux densities are generally a few tenths of a mJy, so given the proximity of the two observing frequencies, we are able to place tighter constraints on our 30 GHz source flux densities by fitting to both datasets, which is particularly useful for sources with poor GBT data. In addition, we are able to identify variable sources and estimate the effect on our SZ measurements.

Most source flux densities are well constrained by a combination of GBT and OVRO/BIMA data. We fit a power law to the measurements in the four GBT frequency sub-bands, plus the interferometer data at 28.5 GHz. For sources with good GBT data, the Coble et al. points serve as a valuable check for variability, but otherwise have minimal effect. In the three cases where significant variability is found, we take the two differing flux density measurements, and use half the difference as an estimate of the uncertainty in our measurement due to variability. We then add this in quadrature to the measurement error. The source exhibiting the greatest variability, source 1 in Abell 2261, has little effect on our results since it lies well away from the cluster centre and data where it lies close to a reference arc are flagged out (Section 5.3). Where no 28.5 GHz flux density is available, we proceed with the GBT data alone. Such cases are unlikely to be crucial, as the non detection by OVRO/BIMA suggests the source is either rather faint, or well away from the central regions of the cluster. Many sources have GBT data which are usable but rather noisy. In such cases, the 28.5 GHz data are invaluable in tying down the 30 GHz flux density due to their comparatively small uncertainties.

Seven sources have no usable GBT data: two in A1835, one in A2219, one in A1763, one in A68 and two in A773. We now discuss our method for each source in turn. Source 1 in A1835 was measured twice by OVRO/BIMA, and also appears in NVSS. We fit a power law to the three measurements. As our observing frequency is close to that of OVRO/BIMA, assuming a constant spectral index is unlikely to have a large impact. We rule out significant variability. Source 2 in A1835 was also measured twice at 28.5 GHz, but does not appear in NVSS. We consult FIRST for a lower frequency measurement, and proceed as for source 1. For source 2 in A2219, we again fit a power law to the OVRO/BIMA and NVSS datapoints. Source 6 in A68 does not appear in any of the lower frequency catalogues but is well measured by OVRO/BIMA. It is outside the OCRA beams so its flux density has only a small effect on the SZ measurement. Both sources in A773 are faint in NVSS and are not detected by OVRO/BIMA. The noise on the OVRO map is 0.078 mJy, giving a 5σ upper limit of 0.39 mJy. As

Table 2. Radio sources found within 5 arcmin of the cluster pointing centre in the NVSS (Condon et al. 1998) and GB6 (Gregory et al. 1996) surveys, and also in the observations of Coble et al. (2007). Notes: All sources were observed with the GBT unless marked (*). 30 GHz flux densities were derived from our GBT measurements plus supplementary information at other frequencies as indicated in the final column (OB for OVRO/BIMA, N for NVSS, G for GB6 and F for FIRST). Quoted errors are $\pm 1\sigma$ (68% confidence interval). Some sources were observed more than once with OVRO/BIMA. Sources showing evidence for variability are marked (V). Sources with apparently negative 30 GHz flux densities are shown in italics: these data were not used to correct the SZ measurements.

Cluster	Src #	RA (J2000)	Dec (J2000)	$S_{1.4}$ (mJy)	$S_{4.85}$ (mJy)	$S_{28.5}$ (mJy)	S_{30} (mJy)	Notes
A1835	1*	14 01 02.1	02 52 41.0	39.3 \pm 1.6	-	3.31 \pm 0.14 2.88 \pm 0.07	2.93 \pm 0.18	OB N
	2*	14 01 00.5	02 51 53.0	1.6 \pm 0.1	-	1.26 \pm 0.14 1.36 \pm 0.08	1.33 \pm 0.07	OB F
ZWCL1953	1	08 50 07.8	36 04 21.7	19.4 \pm 1.2	-	-	0.79 \pm 0.70	GBT
	2	08 50 13.4	36 04 22.4	20.8 \pm 1.0	19.0 \pm 4.0	1.19 \pm 0.17	1.28 \pm 0.16	GBT OB
ZW3146	1	10 23 37.2	04 09 06.4	31.5 \pm 1.0	-	2.03 \pm 0.22 2.12 \pm 0.15	2.35 \pm 0.81	GBT OB
	2	10 23 39.6	04 11 15.4	7.1 \pm 0.5	-	0.41 \pm 0.07	0.33 \pm 0.07	GBT OB
	3	10 23 45.1	04 10 40.7	95.8 \pm 3.4	42.0 \pm 7.0	5.35 \pm 0.18 5.70 \pm 0.10	5.27 \pm 0.11	GBT OB
	4	10 23 45.2	04 11 39.7	3.6 \pm 0.4	-	0.85 \pm 0.10	0.80 \pm 0.10	GBT OB
RXJ1532.9+0005	1	15 32 47.4	30 18 46.0	18.0 \pm 1.0	-	-	1.18 \pm 0.21	GBT
	2	15 32 50.7	30 19 47.6	7.9 \pm 0.5	-	6.58 \pm 0.20	6.56 \pm 0.21	OB N
	3	15 32 53.8	30 20 59.8	22.8 \pm 0.8	20.0 \pm 4.0	3.25 \pm 0.18	3.27 \pm 0.12	GBT OB
	4	15 32 54.31	30 23 01.5	4.4 \pm 0.4	-	-	0.92 \pm 0.21	GBT
	5	15 33 03.42	30 23 47.2	2.6 \pm 0.4	-	-	1.12 \pm 0.50	GBT
A2390	1	21 53 32.4	17 42 19.8	20.9 \pm 1.6	-	Not observed	0.23 \pm 0.12	GBT
	2	21 53 36.8	17 41 44.8	235.3 \pm 8.3	220 \pm 20	Not observed	45.77 \pm 0.10	GBT
	3	21 53 40.3	17 42 56.7	12.2 \pm 1.0	-	Not observed	-0.14 \pm 0.09	GBT
A2219	1	16 40 21.83	46 42 47.8	239.1 \pm 8.3	84.8 \pm 8.0	14.87 \pm 0.17	13.74 \pm 1.00	GBT OB
	2*	16 40 23.83	46 41 47.3	7.9 \pm 1.0	-	0.97 \pm 0.17	0.94 \pm 0.17	OB N
	3	16 40 14.98	46 42 28.7	6.1 \pm 0.5	-	-	0.42 \pm 0.09	GBT
	4	16 39 58.07	46 40 37.2	14.1 \pm 0.5	-	-	0.96 \pm 0.09	GBT
RXJ2129.6+0005	1	21 29 36.61	00 02 35.4	2.2 \pm 0.4	-	-	-0.13 \pm 0.21	GBT
	2	21 29 40.00	00 05 22.9	25.4 \pm 1.2	-	2.33 \pm 0.10	2.04 \pm 0.06	GBT OB
	3	21 29 40.14	00 01 44.4	4.5 \pm 0.5	-	-	0.11 \pm 0.13	GBT
	4	21 29 55.24	00 07 56.9	34.3 \pm 1.8	-	-	2.82 \pm 0.11	GBT
A2261	1	17 22 16.9	32 09 10.5	23.0 \pm 1.5	-	9.32 \pm 0.22 10.48 \pm 0.16	15.58 \pm 3.89	GBT OB (V)
	2	17 22 27.7	32 07 57.8	5.3 \pm 0.5	-	-	0.13 \pm 0.08	GBT
	3	17 22 45.3	32 09 27.0	4.85 \pm 0.5	-	-	0.14 \pm 0.10	GBT
	4	17 22 06.55	32 07 01.7	5.8 \pm 0.4	-	-	0.14 \pm 0.08	GBT
A781	1	09 20 08.51	30 32 14.3	19.9 \pm 0.9	-	-	1.42 \pm 0.60	GBT
	2	09 20 14.12	30 29 02.8	17.9 \pm 0.7	-	-	1.22 \pm 0.53	GBT
	3	09 20 21.75	30 32 27.0	2.7 \pm 0.5	-	-	0.11 \pm 0.18	GBT
	4	09 20 22.90	30 29 45.6	73.1 \pm 2.6	32.0 \pm 5.0	5.33 \pm 0.18	5.35 \pm 0.30	GBT OB
	5	09 20 30.83	30 28 02.1	15.8 \pm 1.6	-	-	-0.07 \pm 0.16	GBT
	6	09 20 47.35	30 28 21.3	5.4 \pm 0.6	-	-	0.08 \pm 0.17	GBT
A697	1	08 42 40.22	36 19 16.4	5.4 \pm 0.5	-	-	1.64 \pm 0.54	GBT
	2	08 42 59.67	36 17 43.7	32.5 \pm 1.4	-	-	1.71 \pm 0.65	GBT

Table 2 – *continued*

Cluster	Src #	RA (J2000)	DEC (J2000)	$S_{1.4}$ (mJy) (NVSS)	$S_{4.85}$ (mJy) (GB6)	$S_{28.5}$ (mJy) (O/B)	S_{30} (mJy) (GBT+)	Notes
A1763	1	13 35 15.60	41 00 25.8	7.9 ± 0.5	-	-	-0.10 ± 0.14	GBT
	2*	13 35 19.86	41 00 04.0	859.2 ± 29.5	225 ± 20	31.30 ± 0.41	29.49 ± 0.38	OB G N
A68	1	00 36 52.94	09 05 21.7	22.8 ± 0.8	-	-	1.57 ± 0.05	GBT
	2	00 37 05.21	09 13 33.6	4.4 ± 0.4	-	-	0.60 ± 0.05	GBT
	3	00 37 06.35	09 07 30.4	40.2 ± 1.3	-	1.20 ± 0.12	1.21 ± 0.06	GBT OB
	4	00 37 07.71	09 08 24.0	59.1 ± 2.2	-	1.60 ± 0.10	1.65 ± 0.05	GBT OB
	5	00 37 17.93	09 06 30.5	3.2 ± 0.6	-	-	-0.05 ± 0.04	GBT
	6*	00 37 07.00	09 07 58.7	-	-	1.38 ± 0.11	-	OB
A520	1	04 54 01.11	02 57 45.6	6.3 ± 0.5	-	7.83 ± 0.25	5.75 ± 1.74	GBT OB (V)
						4.42 ± 0.88		
	2	04 54 03.72	02 56 01.9	7.7 ± 1.7	-	-	0.49 ± 0.15	GBT
	3	04 54 12.41	02 57 52.3	7.1 ± 0.5	-	-	-0.15 ± 0.16	GBT
	4	04 54 17.14	02 55 33.5	14.1 ± 1.0	-	0.84 ± 0.11	0.90 ± 0.08	GBT OB
						1.09 ± 0.09		
	5	04 54 21.16	02 55 01.4	26.5 ± 1.6	-	1.00 ± 0.13	0.63 ± 0.10	GBT OB
						0.74 ± 0.14		
A267	1	01 52 29.46	00 59 31.8	30.0 ± 1.0	-	2.75 ± 0.20	3.12 ± 0.23	GBT OB
	2	01 52 54.58	01 02 08.2	4.2 ± 0.5	-	7.55 ± 0.24	7.05 ± 1.12	GBT OB(V)
						5.53 ± 0.73		
	3	01 52 34.35	01 01 20.5	-	-	-	0.59 ± 0.32	GBT
RXJ0439.0+0715	1	04 39 01.26	07 15 42.6	30.6 ± 1.4	-	1.18 ± 0.16	0.89 ± 0.22	GBT OB
ZWCL7160	1	14 57 08.06	22 20 11.2	13.2 ± 0.6	-	0.95 ± 0.05	0.90 ± 0.06	GBT OB
	2	14 57 08.06	22 20 11.2	3.9 ± 0.4	-	0.99 ± 0.07	0.91 ± 0.08	GBT OB
	3	14 57 15.18	22 20 36.0	16.5 ± 1.3	-	0.96 ± 0.04	0.90 ± 0.06	GBT OB
A773	1*	09 17 45.39	51 43 11.2	2.7 ± 0.5	-	< 0.39	-	Negligible
	2*	09 18 01.81	51 44 11.4	3.1 ± 0.5	-	< 0.39	-	Negligible

the sources in A773 lie well away from the OCRA beams, we are confident that their effects on our data are negligible.

5.3 Source corrections

Due to OCRA-p’s position switching strategy, contaminant radio sources can affect the data by producing a *positive* signal when they lie close to the cluster centre, or a rogue *negative* signal when they lie in the reference beam of the telescope. We simulate the effects of the sources based on their measured positions and flux densities, and the OCRA beam response. We then use the resulting effective flux density to correct the SZ data. Contamination through sources at 30 GHz is generally low for bright clusters, producing only small corrections to the SZ data, and thus introduces little bias as a result of the limitations of the method employed. Although we are confident that residual biases are below the level of our errors, we recognise that the absence of 30 GHz data is a limitation in some cases, and there may be additional issues to do with source variability. For clusters where

radio sources fall in the OCRA reference beams, we are able to perform an additional check by flagging out contaminated data based on the range of parallactic angles affected by the source in question. We compare the flagged data with the corrected data, and adjust our final measurement error accordingly.

We recognise that our strategy may miss sources which are important at 30 GHz. The flux limit of NVSS is ~ 2.5 mJy. If we consider a source of flux density ~ 2.4 mJy at 1.4 GHz, and assume a typical spectral index of -0.7 , extrapolating to 30 GHz gives a flux density of 0.34 mJy. Even if such a source were to be located in the central regions of a cluster, the effect on our measurement would still be small relative to random errors. Not all sources have typical spectral indices, but we note that in the 16 clusters additionally observed by Coble et al. (2007), only 1 ‘new’ source, i.e. a source not previously identified in NVSS, was found. However, the quality of our knowledge of the population of sources with mJy flux densities at 30 GHz is poor. We were able to run an additional check for ‘new’ sources lying

in OCRA-p’s reference arcs. We binned the data by parallactic angle to look for contaminating sources that might produce false SZ effects. Although this subdivides the data, and so leads to a noise level that is higher by a factor of 2 – 3 than the central measured flux density averaged over all parallactic angles, no previously uncatalogued sources were detected.

6 X-RAY DATA

6.1 Deriving cluster parameters

Our sample has 15 clusters in common with an upcoming X-ray paper, Giles et al. (in prep), some results from which were made available in advance for this work. The remaining two clusters (ZWCL1953 and RXJ1532.9+3021, which lie outside Giles et al.’s specified redshift range of $0.15 < z < 0.30$) were analysed using an identical method. The authors use *Chandra* ACIS-I and ACIS-S imaging and spectroscopy for each cluster as available via the archive. For the data preparation, they follow closely the method outlined in Maughan et al. (2008). The *Chandra* analysis package used was CIAO¹ version 4.2 and calibration database CALDB 4.1.4. As in Maughan et al. (2008), blank sky, rather than local, backgrounds are used because the clusters fill a large fraction of the field of view.

We fit a gas density model by converting the observed surface brightness profile into a projected emissivity profile, which was then modelled by projecting the modified β -model of Vikhlinin et al. 2006 along the line of sight (see Maughan et al. 2008 for details). Gas parameters and errors were determined from Monte Carlo realisations of the projected emissivity profile. At each data point a new randomised point was drawn from a Gaussian distribution centered on the model value at that point, with a standard deviation equal to the fractional measurement error on the original data point, multiplied by the model value. The error bar on this new randomised point was set to the same fractional size as the error bar on the original observed point.

The cluster temperature, gas mass and R_{500} (the radius enclosing a mean density of 500 times the critical density at the cluster’s redshift) were then determined iteratively. The procedure followed was to extract a spectrum from within an estimated R_{500} (with the central 15% of that radius excluded), integrate the gas density profile to determine the gas mass within the estimated R_{500} , and thus calculate Y_X which is the product of kT and the gas mass, and a low scatter proxy for total mass (Kravtsov et al. 2006). A new value of R_{500} was then estimated from the Y_X - M scaling relation of Vikhlinin et al. (2009),

$$M_{500} = E(z)^{-2/5} A_{YM} \left(\frac{Y_X}{3 \times 10^{14} M_\odot \text{keV}} \right)^{B_{YM}}, \quad (1)$$

with $A_{YM} = 5.77 \times 10^{14} h^{1/2} M_\odot$ and $B_{YM} = 0.57$. Here, M_{500} is the mass within R_{500} (allowing R_{500} to be trivially computed), and

$$E(z) = \sqrt{\Omega_M(1+z)^3 + (1 - \Omega_M - \Omega_\Lambda)(1+z)^2 + \Omega_\Lambda} \quad (2)$$

describes the redshift evolution of the Hubble parameter. This Y_X - M relation assumes self-similar evolution (as $E^{-2/5}$), which has been shown to be a good description of observed clusters to $z \approx 0.6$ (Maughan 2007). The process was repeated until R_{500} converged. In these spectral fits, the source emission was modelled with an absorbed thermal plasma APEC model in the 0.6–9 keV band, with the absorbing column fixed at the Galactic value. N_H values were taken from the HI map by Kalberla et al. (2005).

Our final cluster parameters, with T_X , L_X and Y_X determined within a radius of R_{500} are given in Table 3.

6.2 β -model fitting

As mentioned in Section 4.1, the small separation of the OCRA-p beams relative to the extent of a cluster’s SZ decrement implies that we subtract out a fraction of the SZ signal due to our differencing method. This significantly reduces the measured signal compared to the intrinsic central signal. This is further exaggerated in cases where we have adjusted the pointing centre to avoid bright radio sources. In order to remove this effect and recover the ‘true’ SZ signal, we model the cluster atmosphere and estimate the fraction of the signal ‘missed’. (Note: this analysis was conducted purely to correct the SZ measurements and is separate from the derivation of X-ray cluster parameters discussed in Section 6.1). In our previous work (Lancaster et al. 2007), we assumed that the gas density distribution, $n_e(r)$ was well fit by a standard spherical β -model (Cavaliere & Fusco-Femiano 1976):

$$n_e(r) = n_{e0} \left(1 + \frac{r^2}{r_c^2} \right)^{-3\beta/2} \quad (3)$$

Here, we improve on this approach by also considering the double β -model, which may provide a better fit to clusters which exhibit peaked central emission due to their cool cores. We follow Bonamente et al. (2006) in adopting the form

$$n_e(r) = n_{e0} \left[p \left(1 + \frac{r^2}{r_{c1}^2} \right)^{-3\beta_1/2} + (1-p) \left(1 + \frac{r^2}{r_{c2}^2} \right)^{-3\beta_2/2} \right] \quad (4)$$

although in our analysis, we allow different β for the two components. Using the *SHERPA*² modelling and fitting application for each set of cluster data, we fit the 1-D radial profiles of the X-ray surface brightness by three models:

- (i) The standard single β -model, (3)
- (ii) A double β -model, (4), with $\beta_1 = \beta_2$
- (iii) A double β -model, (4), allowing β_1 and β_2 to assume different values.

Chi squared (χ^2) statistics are used to compare the fits, since each radial bin is based on a large number of X-ray counts. For each cluster, we accept the simplest model for which the fit statistic implies a probability of getting a greater

¹ <http://cxc.harvard.edu/ciao/>

² <http://cxc.harvard.edu/sherpa/>

Table 3. *Chandra* X-ray parameters for the sample, derived inside R_{500} with the central 15% excluded. L_X is the bolometric luminosity. Quoted errors are $\pm 1\sigma$ (68% confidence interval).

Cluster	T_X (keV)	L_X ($10^{45} \text{ ergs}^{-1}$)	Y_X ($10^{15} \text{ M}_\odot \text{ keV}$)	R_{500} Mpc
A1835	$8.41^{+0.32}_{-0.26}$	2.14 ± 0.01	$1.20^{+0.05}_{-0.04}$	1.40
ZW1953	$6.05^{+0.51}_{-0.50}$	1.45 ± 0.05	$0.58^{+0.05}_{-0.05}$	1.19
ZW3146	$7.09^{+0.35}_{-0.37}$	1.62 ± 0.02	$0.77^{+0.04}_{-0.04}$	1.27
RXJ1532.9+3021	$5.62^{+0.72}_{-0.58}$	1.23 ± 0.05	$0.45^{+0.06}_{-0.06}$	1.11
A2390	$10.20^{+0.35}_{-0.35}$	2.87 ± 0.05	$1.79^{+0.06}_{-0.07}$	1.53
A2219	$10.33^{+0.43}_{-0.44}$	3.32 ± 0.04	$2.10^{+0.09}_{-0.09}$	1.58
RXJ2129.6+0005	$6.04^{+0.53}_{-0.52}$	1.03 ± 0.04	$0.52^{+0.05}_{-0.06}$	1.20
A2261	$6.56^{+0.28}_{-0.28}$	1.46 ± 0.02	$0.77^{+0.03}_{-0.03}$	1.31
A781	$5.32^{+0.66}_{-0.43}$	1.02 ± 0.05	$0.53^{+0.06}_{-0.04}$	1.18
A697	$9.22^{+0.66}_{-0.65}$	2.70 ± 0.05	$1.55^{+0.11}_{-0.11}$	1.45
A1763	$7.31^{+0.47}_{-0.47}$	1.48 ± 0.03	$0.89^{+0.06}_{-0.06}$	1.34
A68	$7.14^{+0.88}_{-0.78}$	1.09 ± 0.04	$0.60^{+0.07}_{-0.07}$	1.23
A520	$6.78^{+0.29}_{-0.16}$	1.49 ± 0.02	$0.74^{+0.03}_{-0.02}$	1.31
A267	$4.53^{+0.49}_{-0.38}$	0.75 ± 0.05	$0.29^{+0.03}_{-0.03}$	1.08
RXJ0439.0+0715	$5.32^{+0.38}_{-0.29}$	1.58 ± 0.04	$0.57^{+0.04}_{-0.04}$	1.23
ZW7160	$4.64^{+0.18}_{-0.18}$	0.69 ± 0.01	$0.28^{+0.01}_{-0.01}$	1.06
A773	$6.75^{+0.40}_{-0.26}$	1.13 ± 0.02	$0.65^{+0.03}_{-0.03}$	1.27

χ^2 by chance, $Q \geq 6$ per cent. For some clusters, the gas distribution is sufficiently disturbed that $Q < 6$ per cent for all models fitted: in such cases we adopt the best fit. This is not ideal, but we expect the additional error to be at a low level in comparison with the random errors on the SZ data. We do not observe any systematic effect on our results due to the type of β -model used to correct the SZ data.

β -model parameters are presented in Table 4. We return briefly to the analysis of Bonamente et al. (2006), with whom we have eight clusters in common, for comparison of results. For A697, A68, A267 and A773, both groups find that a single β -model provides an acceptable fit, and the derived parameters are in broad agreement. For their double β -model fits, Bonamente et al. fix the two values to β to be equal, whereas ours were allowed to vary. For RXJ2129.6+0005 and A2261, we find that a model with $\beta_1 = \beta_2$ gives the best fit, and the model parameters are again in broad agreement with Bonamente et al. For ZWCL3146, our two β -values differ but are very similar, meaning the overall model fit is in broad agreement with Bonamente et al., and indeed our $\beta_1 = \beta_2$ fit is also consistent. The exception is A1835, where we find the best fitting model to be a double β -model with $\beta_1 = 0.675$, $\beta_2 = 1.059$, $\theta_1 = 35.6$ arcsec and $\theta_2 = 13.2$ arcsec, whereas Bonamente et al. find $\beta = 0.797$, $\theta_1 = 63.6$ arcsec and $\theta_2 = 13.2$ arcsec. Our model with $\beta_1 = \beta_2$ is also slightly discrepant, as our best fit parameters are $\beta = 0.695$, $\theta_1 = 92.1$ arcsec and $\theta_2 = 19.1$ arcsec. The source of discrepancy may well be in the use of differing data sets. We use ACIS-I observations totalling 200ks, whereas Bonamente et al. only had access to 30ks of ACIS-S data which has a significantly smaller field of view.

We use the model gas distribution to simulate an OCRA observation. Many clusters were observed at posi-

tions slightly shifted from their X-ray maxima in order to avoid bright radio sources as far as possible. We consult our OCRA data for the range of parallactic angles sampled, and include the convolution with the OCRA beam response. We can thus estimate the fraction F of the ‘true’ SZ signal measured in the real observations, and ‘correct’ our measurement (multiply by $1/F$) to recover the SZ surface brightness that would be measured by an ideal instrument with narrow beams at infinite separation. We note for clusters where the double β -model provides an improved fit, the value of F varies from the simpler single β -model by ~ 10 per cent. This change is thus significant for the scientific interpretation of our results. Correction factors are presented in Table 5. Asymmetries in the SZ signal are assumed small in our analysis. Checks for such asymmetries by binning the SZ data by parallactic angle provide only a low signal-to-noise control against such effects which would cause our estimates of F to be incorrect. The X-ray isophotes of these clusters are not always circular, but are most sensitive to asymmetry towards the cluster centre, where a relatively small fraction of the SZ effect originates. We estimate that the value of F could be systematically uncertain by 20% from this effect. This uncertainty dominates over that from varying the density model from β or double- β form to the Vikhlinin et al. (2006) form.

7 RESULTS AND SCALING RELATIONS

7.1 Sunyaev Zel’dovich Results

We present our measurements for the Sunyaev Zel’dovich effects in our 17-cluster sample in Table 5. For each cluster, we first give the raw OCRA flux density as measured directly by the telescope, followed by the revised figure once all ra-

Table 4. β -model parameters for the cluster sample. The best fitting model is shown for each cluster, where the parameter p indicates the fraction of each component as described by Equation 4. Quoted errors are $\pm 1\sigma$ (68% confidence interval). In cases where a double- β model provided the best fit, we choose the larger of the core radii to be r_{c1} . The resulting correction factors applied to the SZ data are given in Table 5.

Cluster	β_1	r_{c1} (arcsec)	β_2	r_{c2} (arcsec)	p
A1835	$0.675^{+0.001}_{-0.001}$	$35.6^{+0.6}_{-0.6}$	$1.059^{+0.010}_{-0.010}$	$13.2^{+0.1}_{-0.1}$	0.10
ZWCL1953	$0.972^{+0.147}_{-0.122}$	$171.6^{+22.3}_{-21.9}$	$0.972^{+0.147}_{-0.122}$	$43.3^{+5.7}_{-5.1}$	0.04
ZWCL3146	$0.700^{+0.008}_{-0.007}$	$23.6^{+0.9}_{-0.8}$	$0.652^{+0.032}_{-0.023}$	$4.8^{+0.3}_{-0.2}$	0.14
RXJ1532.9+3021	$0.650^{+0.011}_{-0.010}$	$12.0^{+3.6}_{-1.7}$	$0.650^{+0.011}_{-0.010}$	$6.3^{+1.6}_{-1.8}$	0.40
A2390	$0.831^{+0.010}_{-0.009}$	$92.9^{+1.6}_{-1.6}$	$0.831^{+0.010}_{-0.009}$	$18.5^{+0.3}_{-0.3}$	0.10
A2219	$0.725^{+0.015}_{-0.013}$	$85.6^{+6.2}_{-5.0}$	$0.725^{+0.015}_{-0.013}$	$42.0^{+5.4}_{-5.6}$	0.58
RXJ2129.6+0005	$0.609^{+0.011}_{-0.011}$	$24.4^{+2.9}_{-2.5}$	$0.609^{+0.011}_{-0.011}$	$5.0^{+0.8}_{-0.7}$	0.12
A2261	$0.598^{+0.003}_{-0.003}$	$30.7^{+1.4}_{-1.4}$	$0.598^{+0.003}_{-0.003}$	$11.8^{+0.8}_{-0.8}$	0.33
A781	$0.706^{+0.041}_{-0.035}$	$79.5^{+7.5}_{-6.6}$	-	-	-
A697	$0.648^{+0.008}_{-0.008}$	$48.7^{+1.5}_{-1.5}$	-	-	-
A1763	$0.586^{+0.007}_{-0.006}$	$48.0^{+1.6}_{-1.6}$	-	-	-
A68	$0.742^{+0.003}_{-0.002}$	$54.5^{+3.5}_{-3.3}$	-	-	-
A520	$0.831^{+0.003}_{-0.003}$	$117.5^{+0.6}_{-0.6}$	-	-	-
A267	$0.633^{+0.011}_{-0.011}$	$34.4^{+1.5}_{-1.4}$	-	-	-
RXJ0439.0+0715	$0.735^{+0.022}_{-0.020}$	$52.6^{+4.3}_{-3.9}$	$0.735^{+0.022}_{-0.020}$	$13.0^{+1.6}_{-1.5}$	0.23
ZWCL7160	$0.850^{+0.112}_{-0.077}$	$22.2^{+4.3}_{-3.4}$	$0.580^{+0.005}_{-0.006}$	$7.2^{+0.3}_{-0.4}$	0.09
A773	$0.769^{+0.041}_{-0.035}$	$129.6^{+14.3}_{-14.4}$	$0.769^{+0.041}_{-0.035}$	$48.2^{+2.7}_{-2.6}$	0.11

dio source contamination has been corrected for. We then give our estimate of the fraction of total signal measured due to the instrumental response. Finally, we give the fully-corrected temperature decrement expressed in brightness temperature units, and the corresponding central Comptonisation parameter, $y_0 = -0.19 \times (\Delta T/K)$. We detect 13 clusters at significance $\geq 3\sigma$.

Our trail fields serve as a valuable test of our observing strategy. We present differential and cumulative distributions for both the source corrected cluster target and trail fields in Figure 1. The flux densities of the trail fields are distributed around zero with small scatter, and their distribution is clearly distinct from that of the SZ data, confirming that our observing strategy is effective.

7.2 SZ-X-ray scaling relations

According to the self-similar model of galaxy cluster formation, which assumes evolution solely under gravity, we expect simple scalings between various cluster parameters. Following Morandi et al. (2007) we derive the following relations, each of which may be tested using OCRA data. We note that while it is advantageous to use the integrated Compton parameter for such studies (e.g. Benson et al. 2004, Bonamente et al. 2008), deriving this from OCRA data would introduce further uncertainty since we have measured the cluster structures from the X-ray data alone. Thus, we restrict ourselves to discussing the central Comptonisation, y_0 . The scalings of interest are first, the relation between central Comptonisation and X-ray temperature

$$y_0 \propto T_X^{3/2} E(z), \quad (5)$$

second, that between the Comptonisation and X-ray luminosity

$$y_0 \propto L_X^{3/4} E(z)^{1/4}, \quad (6)$$

and finally, that between Comptonisation and Y_X , the product of gas mass and X-ray temperature

$$y_0 \propto Y_X^{3/5} E(z)^{8/5}, \quad (7)$$

where $E(z)$ is as given in Equation 2. Deviation from the expected scalings would suggest contributions from non-gravitational processes, and redshift dependence in the slope or amplitude of the scalings should provide evidence on the nature of these processes.

We present our scaling relations in figures 2(a) to 2(c). For each plot, we colour-code the datapoints based on the reliability of the OCRA data. The most reliable points, i.e. those with no obvious issues, are shown as red circles. Points which have a signal to noise ratio of less than 3 are black squares. This is an arbitrary cut-off, and we see no reason to exclude these points from our analysis; however as an aid to the reader we choose to mark them clearly. Blue crosses represent clusters which may suffer from residual source contamination, i.e. those which contain a bright (> 3 mJy) source, for which we have corrected, in their central regions. Due to the unavoidable 10 per cent uncertainty in the calibration of the GBT data, we cannot be confident that the effects of these sources have been accurately removed, and thus choose to ignore these three clusters in our subsequent analyses.

The fitting was performed in the linear space of observ-

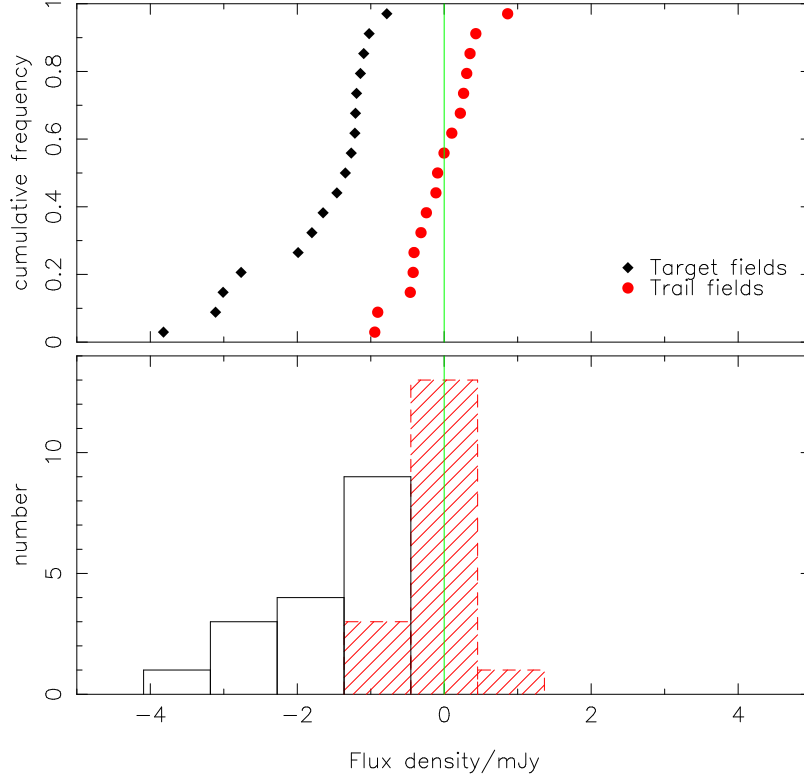
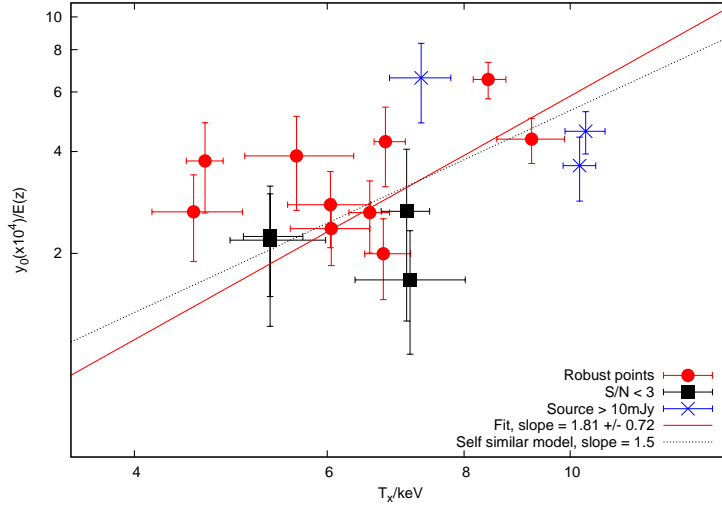


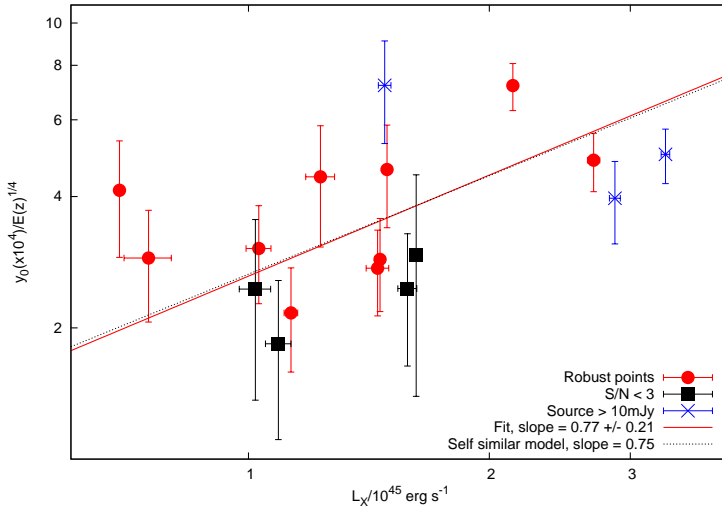
Figure 1. Lower panel: histogram of the source-corrected flux densities for the target cluster fields (black solid lines) and the flux densities for the reference trail fields (red dashed lines with cross-hatching). Upper panel: the corresponding cumulative distributions for the clusters (black diamonds) and the trail fields (red circles). Note that the trail field flux densities are consistent with zero, suggesting that our switching scheme removes atmospheric and ground-based contamination effectively. The cluster and trail field flux density distributions clearly differ.

Table 5. OCRA SZ measurements. S_{Raw} gives the raw OCRA measurement, whereas S_{SC} is the SZ flux after correction for contaminant point sources. The fourth column lists the measured fractions of the expected SZ signal due to the OCRA switching pattern. ΔT is the brightness temperature decrement, corrected for point sources and the instrumental response. All errors are $\pm 1\sigma$ (68% confidence interval).

Cluster	S_{Raw} (mJy)	S_{SC} (mJy)	Fraction Measured	ΔT (μK)	y_0 $\times 10^4$
A1835	-2.05 ± 0.46	-3.82 ± 0.47	0.363	-4050 ± 500	7.70 ± 0.95
ZW1953	-1.65 ± 0.37	-1.65 ± 0.37	0.404	-1570 ± 350	2.98 ± 0.67
ZW3146	-1.06 ± 0.39	-0.78 ± 0.41	0.181	-1660 ± 870	3.15 ± 1.65
RX1532.9+3021	-1.41 ± 0.33	-1.11 ± 0.34	0.166	-2540 ± 790	4.83 ± 1.50
A2390	-0.78 ± 0.20	-1.02 ± 0.22	0.176	-2230 ± 480	4.24 ± 0.91
A2219	11.10 ± 0.38	-2.76 ± 0.40	0.379	-2810 ± 400	5.34 ± 0.76
RXJ2129.6+0005	-0.13 ± 0.37	-1.46 ± 0.37	0.329	-1710 ± 430	3.25 ± 0.82
A2261	-3.19 ± 0.30	-1.35 ± 0.32	0.321	-1610 ± 390	3.06 ± 0.74
A781	0.68 ± 0.42	-1.19 ± 0.53	0.330	-1390 ± 620	2.64 ± 1.18
A697	-3.01 ± 0.46	-3.01 ± 0.46	0.422	-2740 ± 420	5.21 ± 0.80
A1763	10.58 ± 0.80	-3.11 ± 0.82	0.296	-4040 ± 1070	7.68 ± 2.03
A68	-0.89 ± 0.48	-1.22 ± 0.48	0.451	-1040 ± 410	1.98 ± 0.78
A520	-1.97 ± 0.47	-1.80 ± 0.48	0.268	-2580 ± 680	4.90 ± 1.29
A267	-2.73 ± 0.43	-1.99 ± 0.57	0.471	-1620 ± 470	3.08 ± 0.89
RX0439.0+0715	-1.22 ± 0.43	-1.27 ± 0.43	0.351	-1390 ± 470	2.64 ± 0.89
ZWCL7160	-1.10 ± 0.34	-1.14 ± 0.34	0.188	-2330 ± 700	4.43 ± 1.33
A773	-1.20 ± 0.32	-1.21 ± 0.32	0.382	-1210 ± 330	2.30 ± 0.63



(a) X-ray temperature



(b) X-ray luminosity

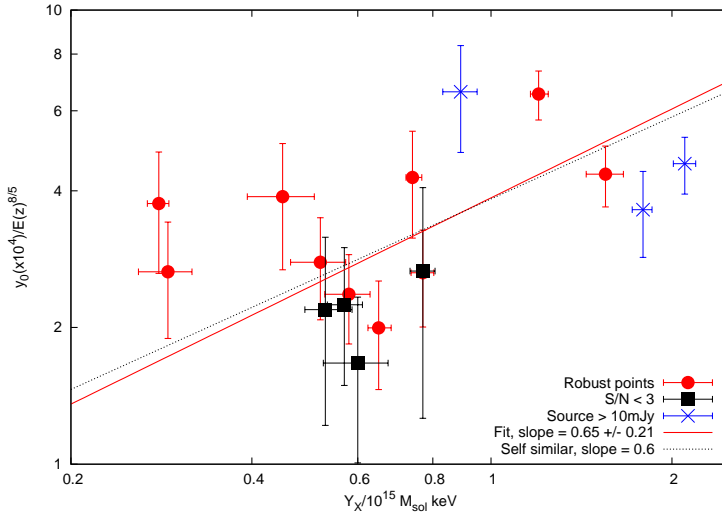
(c) Y_X parameter

Figure 2. Scaling relations between the central Comptonisation as derived from OCRA data and various X-ray parameters. We fit to the ‘robust’ and ‘low significance’ data (red circles and black squares respectively), but omit the clusters with potential residual source contamination (blue crosses); the best-fit result is shown as the solid red line. The dotted black line depicts the expectation from self-similar evolution.

Table 6. Best-fit slopes for the correlations examined in Sections 7.2 and 7.3, along with the expectations from self-similar models for comparison. For the SZ/X-ray scalings, we give results for the analysis both with and without corrections for contaminant radio sources in the OCRA data. We note that the fits are significantly poorer where the source corrections are omitted. All fits are consistent with predictions from self-similar models of cluster formation.

Correlation	Expected slope	Data used	Best-fit slope	Fit statistic
y_0, T_X	1.5	SZ, X-ray	1.82 ± 0.72	2.39
		SZ (no source correction), X-ray	1.94 ± 1.10	6.64
y_0, L_X	0.75	SZ, X-ray	0.77 ± 0.21	2.46
		SZ (no source correction), X-ray	0.71 ± 0.19	6.86
y_0, Y_X	0.6	SZ, X-ray	0.65 ± 0.21	2.50
		SZ (no source correction), X-ray	0.55 ± 0.21	7.23
L_X, T_X	0.5	X-ray only	0.49 ± 0.04	3.40
Y_X, T_X	2.5	X-ray only	2.19 ± 0.16	1.85
Y_X, L_X	1.25	X-ray only	1.24 ± 0.05	4.29

ables, rather than log-log space, and involved the minimisation of the squared and error-weighted residuals from a power law of the form $y = Ax^B$, where A and B are to be estimated. The space of acceptable values of A and B was sampled by taking 10^5 datapoint realisations, distributed according to their errors, assumed Gaussian. The best-fit slopes are summarised in Table 6, with the values of the fit statistic. Figure 2(a) shows the scaling between y_0 and T_X . For this relation, the space of acceptable (A, B) parameters extends over a wide range in both parameters, so that the slope should be regarded as essentially unconstrained, although the best fit value $B = 1.82 \pm 0.72$ is in agreement with the predicted value $B = 1.5$ from self-similar models. The other two relations show modest covariances between A and B and are more robust. Figure 2(b) shows the scaling between y_0 and L_X . We obtain a slope of 0.77 ± 0.21 in good agreement with self-similarity, for which Equation 6 predicts 0.75. Finally, Figure 2(c) depicts the scaling between y_0 and Y_X . We derive a slope of 0.65 ± 0.21 which is in good agreement with the predicted $B = 0.6$. For all three cases, the intrinsic scatter in y_0 can be estimated by the additional error required to bring the fit statistic down to a statistically acceptable level ~ 1.0 . We find that the intrinsic scatter in y_0 is about 25 per cent. The errors on B are large for all fits because of the modest range of cluster masses in our sample, but we see no evidence for departure from self-similar models of cluster evolution. Our results for the y_0/L_X and y_0/T_X scalings are consistent with those obtained by Morandi et al. (2007), although their gas masses and temperatures were defined over significantly different regions of the clusters (within R_{2500}), and their scalings have smaller slope errors because of the wider range of T_X of their clusters.

It is interesting to compare our scalings with those that we would have obtained if source corrections were not available to us, since blank-sky surveys for cluster SZ effects could attempt to constrain the scalings with inadequate source data. We find that the scatter induced by the radio sources degrades the fit quality for each correlation significantly, as illustrated by the fit statistics shown in Table 6. Although the results broadly agree with self-similar predictions, the residual contamination tends to cause the scalings

to appear too flat. For instance, in the high signal to noise sub-sample where the effect of sources is clearest, the slope of the y_0/L_X relation is found to be flatter by 0.27 if a fit is attempted before source corrections are made. A similar result is found for the y_0/Y_X scaling relation.

7.3 X-ray only scaling relations

We check the consistency of the set of clusters with the more usual X-ray scaling relations between L_X and T_X , Y_X and T_X , and Y_X and L_X (e.g. Morandi et al. 2007) in the same way as for the SZ / X-ray scaling relations (results also summarised in Table 6). The slopes that we measure, of 0.49 ± 0.04 , 2.19 ± 0.16 , and 1.24 ± 0.05 , are consistent with the similarity expectations of 0.5, 2.5 and 1.25. As the slight discrepancy for the correlation between Y_X and T_X is not of high statistical significance, this study shows our sample to be representative of the population of hot ($T \gtrsim 6$ keV) clusters.

8 DISCUSSION AND CONCLUSION

We have observed a complete sample of galaxy clusters using OCRA-p, and studied the scaling of the central Compton parameter, y_0 , with various X-ray quantities. For each relation, we find slopes in good agreement with the predictions from self-similar models.

Our study has similarities to that of Morandi et al. (2007), and the two samples have 7 clusters in common, although we imposed stricter initial selection criteria. Morandi et al. consider scalings with y_0 , so we are able to perform a direct comparison. They find that the y_0/T_X relation deviates by $\sim 3\sigma$ from the self-similar prediction, in the sense of being steeper. While our data are consistent with this result, we note that they are essentially unable to constrain this relation at any level. Regarding the y_0/L_X scaling, they find a slope of 0.61 ± 0.05 , which is in good agreement with our work. Thus we see no sign of the flattening that would have resulted from the presence of an undetected set of contaminating sources (Section 7.2).

More recently, Bonamente et al. (2008) studied a sample of 38 clusters observed with OVRO/BIMA and *Chandra*.

They considered the integrated Comptonisation, Y , and in particular its scaling with T_X , M_{tot} and M_{gas} . They find good consistency with predictions from self-similar models for all scaling relations.

Our analysis has been limited by the narrow region of parameter space sampled, particularly for the scalings with T_X . Based on our results, a sample double the size would provide a good test of the y_0/Y_X scaling; this will be presented in an upcoming paper in which we extend our sample to 33 clusters. To fully test the other relations, a sample four times larger is required. Thinking forwards to the prospects for blind cluster surveys, it is interesting to note that in this study we would have detected Sunyaev Zel'dovich effects for 14 out of 17 clusters in our sample with no source information. Of course, to accurately determine the strength of the SZ effect in each case, and indeed to derive any cluster parameters, good knowledge of the radio source environment is essential, and any attempt to test the scaling relations without taking sources into account will fail (see Section 7.2). That this is true for sub-mm sources, as well as cm-wave studies, is clear from the large population of sub-mm sources known to be lensed by massive clusters (e.g. Johansson et al. 2010).

ACKNOWLEDGMENTS

We acknowledge support for the design and construction of OCRA-p from the Royal Society Paul Instrument Fund, and funds for the data acquisition system and operation on the telescope from the Ministry of Science in Poland via grant number N N203 39043 who, along with STFC, also supported the scientific exploitation of the completed system. The GBT is a National Radio Astronomy Observatory (NRAO) instrument, a facility of the National Science Foundation operated under cooperative agreement by Associated Universities, Inc. We extend special thanks to all the staff at the GBT, particularly Brian Mason and Carl Bignell, for their essential support and prompt re-scheduling.

REFERENCES

- Ade P. A. R., Aghanim N., Arnaud M., Ashdown M., Aumont J., Baccigalupi C., Balbi A., Banday A. J., Barreiro R. B., et al. 2011, ArXiv e-prints
- Bartkiewicz A., Szymczak M., van Langevelde H. J., 2005, A&A, 442, L61
- Benson B. A., Church S. E., Ade P. A. R., Bock J. J., Ganga K. M., Henson C. N., Thompson K. L., 2004, ApJ, 617, 829
- Błaszczewicz L., Kus A. J., 2004, A&A, 413, 233
- Bonamente M., Joy M., LaRoque S. J., Carlstrom J. E., Nagai D., Marrone D. P., 2008, ApJ, 675, 106
- Bonamente M., Joy M. K., LaRoque S. J., Carlstrom J. E., Reese E. D., Dawson K. S., 2006, ApJ, 647, 25
- Browne I. W., Mao S., Wilkinson P. N., Kus A. J., Marecki A., Birkinshaw M., 2000, in Butcher H. R., ed., Proc. SPIE Vol. 4015, p. 299-307, Radio Telescopes, Harvey R. Butcher; Ed. OCRA: a one-centimeter receiver array. pp 299-307
- Cavaliere A., Fusco-Femiano R., 1976, A&A, 49, 137
- Coble K., Bonamente M., Carlstrom J. E., Dawson K., Hasler N., Holzapfel W., Joy M., La Roque S., Marrone D. P., Reese E. D., 2007, AJ, 134, 897
- Condon J. J., Cotton W. D., Greisen E. W., Yin Q. F., Perley R. A., Taylor G. B., Broderick J. J., 1998, AJ, 115, 1693
- Ebeling H., Edge A. C., Bohringer H., Allen S. W., Crawford C. S., Fabian A. C., Voges W., Huchra J. P., 1998, MNRAS, 301, 881
- Gawroński M. P., Peel M. W., Lancaster K., et al., 2010, MNRAS, p. 816
- Gregio L., Carlstrom J. E., Reese E. D., Holder G. P., Holzapfel W. L., Joy M. K., Mohr J. J., Patel S., 2001, ApJ, 552, 2
- Gregory P. C., Scott W. K., Douglas K., Condon J. J., 1996, ApJS, 103, 427
- Huang C., Protty Wu J., Ho P. T. P., et al., 2010, ApJ, 716, 758
- Hughes J. P., Birkinshaw M., 1998, ApJ, 501, 1
- Jarosik N., Bennett C. L., Halpern M., Hinshaw G., Kogut A., Limon M., Meyer S. S., Page L., Pospieszalski M., Spergel D. N., Tucker G. S., Wilkinson D. T., Wollack E., Wright E. L., Zhang Z., 2003, ApJS, 145, 413
- Johansson D., Horellou C., Sommer M. W., Basu K., Bertoldi F., Birkinshaw M., Lancaster K., Lopez-Cruz O., Quintana H., 2010, A&A, 514, A77
- Kalberla P. M. W., Burton W. B., Hartmann D., Arnal E. M., Bajaja E., Morras R., Pöppel W. G. L., 2005, A&A, 440, 775
- Kravtsov A. V., Vikhlinin A., Nagai D., 2006, ApJ, 650, 128
- Lancaster K., Birkinshaw M., Gawroński M. P., Browne I., Feiler R., Kus A., Lowe S., Pazderski E., Wilkinson P., 2007, MNRAS, 378, 673
- Lancaster K., Genova-Santos R., Falcón N., Grainge K., Gutiérrez C., Kneissl R., Marshall P., Pooley G., Rebolo R., Rubiño-Martín J.-A., Saunders R. D. E., Waldram E., Watson R. A., 2005, MNRAS, 359, 16
- LaRoque S. J., Bonamente M., Carlstrom J. E., Joy M. K., Nagai D., Reese E. D., Dawson K. S., 2006, ApJ, 652, 917
- Lowe S., 2005, PhD thesis, University of Manchester
- Lowe S. R., Gawroński M. P., Wilkinson P. N., Kus A. J., Browne I. W. A., Pazderski E., Feiler R., Kettle D., 2007, A&A, 474, 1093
- Mandolesi N., Bersanelli M., Burigana C., Villa F., 2000, Astrophysical Letters Communications, 37, 151
- Marriage T. A., Acquaviva V., Ade a. e., 2010, ArXiv e-prints
- Mason B. S., Myers S. T., Readhead A. C. S., 2001, ApJ, 555, L11
- Mason B. S., Weintraub L., Sievers J., Bond J. R., Myers S. T., Pearson T. J., Readhead A. C. S., Shepherd M. C., 2009, ApJ, 704, 1433
- Maughan B. J., 2007, ApJ, 668, 772
- Maughan B. J., Jones C., Forman W., Van Speybroeck L., 2008, ApJS, 174, 117
- Menanteau F., Gonzalez J., Juin J., et al., 2010, ArXiv e-prints
- Morandi A., Ettori S., Moscardini L., 2007, MNRAS, 379, 518
- Muchovej S., Leitch E., Carlstrom J. E., Culverhouse T., Greer C., Hawkins D., Hennessy R., Joy M., Lamb J., Loh

- M., Marrone D. P., Miller A., Mroczkowski T., Pryke C., Sharp M., Woody D., 2011, *ApJ*, 732, 28
- Pazderska B. M., Gawroński M. P., Feiler R., Birkinshaw M., Browne I. W. A., Davis R., Kus A. J., Lancaster K., Lowe S. R., Pazderski E., Peel M., Wilkinson P. N., 2009, *A&A*, 498, 463
- Peel M., 2009, PhD thesis, University of Manchester
- Reese E. D., Carlstrom J. E., Joy M., Mohr J. J., Grego L., Holzapfel W. L., 2002, *ApJ*, 581, 53
- Saunders R., Kneissl R., Grainge K., Grainger W. F., Jones M. E., Maggi A., Das R., Edge A. C., Lasenby A. N., Pooley G. G., Miyoshi S. J., Tsuruta T., Yamashita K., Tawara Y., Furuzawa A., Harada A., Hatsukade I., 2003, *MNRAS*, 341, 937
- Staniszewski Z., Ade P. A. R., Aird K. A., et al., 2009, *ApJ*, 701, 32
- Sunyaev R. A., Zel'dovich Y. B., 1972, *Comments on Astrophysics*, 4, 173
- Vanderlinde K., Crawford T. M., de Haan T., et al., 2010, *ArXiv e-prints* 1003.0003
- Vikhlinin A., Burenin R. A., Ebeling H., Forman W. R., Hornstrup A., Jones C., Kravtsov A. V., Murray S. S., Nagai D., Quintana H., Voevodkin A., 2009, *ApJ*, 692, 1033
- Vikhlinin A., Kravtsov A., Forman W., Jones C., Markevitch M., Murray S. S., Van Speybroeck L., 2006, *ApJ*, 640, 691
- Voges W., Aschenbach B., Boller T., et al., 1999, *A&A*, 349, 389
- Wright E. L., Chen X., Odegard N., et al., 2009, *ApJS*, 180, 283
- Zwart J. T. L., Barker R. W., Biddulph P., et al., 2008, *MNRAS*, 391, 1545

This paper has been typeset from a \LaTeX file prepared by the author.